

pubs.acs.org/cm Article

# Synthetic Strategies, Thermal Stability, and Optical Properties for Nanostructured Famatinite with Cu-Site Doping

Mitchel S. Jensen, Katherine E. Plass, and Mary E. Anderson\*



Cite This: Chem. Mater. 2022, 34, 9086–9097



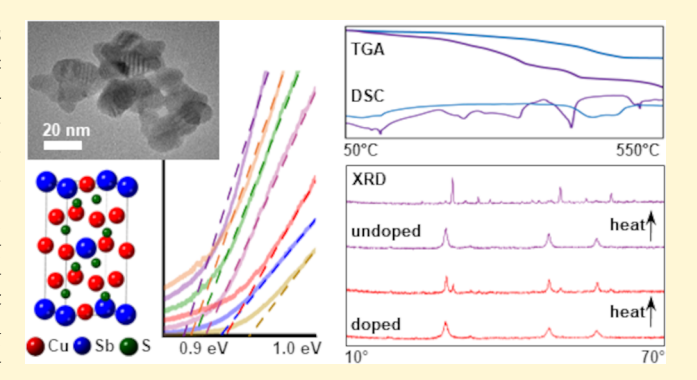
**ACCESS** 

III Metrics & More

Article Recommendations

s Supporting Information

ABSTRACT: A copper—antimony—sulfide phase known as famatinite ( $Cu_3SbS_4$ ), with desirable properties for photovoltaic and thermoelectric applications, has been synthesized using a solution-phase technique that is energy-efficient and surfactant-free. The modified polyol process produced phase-pure nanoparticles (20-30 nm diameter) and allowed the facile incorporation of a range of Cu-site dopants (Fe, Ni, Zn, and Mn). Synthetic optimization identified the ideal reaction time and temperature to produce phase-pure famatinite and revealed covellite (CuS) as the primary growth intermediate. The effect of Cu-site dopants and nanostructuring on the thermal and optical properties was investigated. Thermogravimetric analysis and differential scanning calorimetry showed that doping the nano-



particles on the Cu-site improved thermal stability to be comparable with larger particles. Decomposition analysis by X-ray diffraction (XRD) and energy-dispersive X-ray spectroscopy (EDS) further demonstrated the stability of famatinite with Cu-site dopants and identified sulfur loss as a major factor in the phase transition of famatinite to tetrahedrite ( $Cu_{12}Sb_4S_{13}$ ) upon annealing. Optical characterization of famatinite revealed a direct  $\sim$ 0.9 eV band gap regardless of dopant. Dispersibility of famatinite nanoparticles was tailored for different solvents by post-synthetic surface functionalization. The combination of thermal stability, favorable optical properties, and processability demonstrated herein affords famatinite materials with tunable properties for application in solar cells and thermoelectric devices.

#### ■ INTRODUCTION

Power generation is a major source of CO<sub>2</sub> emissions, so the development of materials for solar energy conversion and thermoelectric power generation is a key avenue towards more sustainable energy. Crystalline silicon is the dominant solar cell technology in use with a single-junction conversion efficiency  $(\eta)$  of up to 26.3%. Due to the high costs of the silicon solar cell manufacturing process, other options are being investigated. Furthermore, the indirect band gap of silicon results in lower light absorption, which decreases the suitability for thin film applications.<sup>3</sup> Efforts to identify alternatives have focused on direct band gap chalcogenide materials like  $CuIn_{1-\nu}Ga_{\nu}Se_{2}$  (CIGS) and  $Cu_{2}ZnSnS_{4}$  (CZTS), with  $\eta =$ 22 and 10%, respectively. 4-6 The low elemental abundance and high material cost are drawbacks of CIGS, whereas challenges that plague the synthesis of CZTS include the production of multiple competitive phases and cation disorder.<sup>7,8</sup> Chalcogenide materials are also studied for thermoelectric applications, with promising examples including PbTe (ZT = 2.5 at 923 K)<sup>9</sup> and Bi<sub>0.5</sub>Sb<sub>1.5</sub>Te<sub>3</sub> materials (ZT = 1.86 at 320 K). The dimensionless figure of merit Z is given as  $ZT = (S^2 \sigma / \kappa) T$ , where S is the Seebeck coefficient,  $\sigma$ is the electrical conductivity,  $\kappa$  is the thermal conductivity, and T is the absolute temperature. 11 Derivatives of PbTe and

 $Bi_2Te_3$  have demonstrated high efficiency as thermoelectrics and have seen commercial adoption,  $^{12,13}$  but the low elemental abundance, cost, and toxicity of these products continue to limit their widespread use.  $^{13}$  The copper—antimony—sulfide (CAS) subset of materials is composed of low-cost, earth-abundant compounds with properties rendering them suitable for photovoltaic and thermoelectric applications.  $^{14-19}$  The CAS system features four main compounds: tetrahedrite (Cu $_{12}{\rm Sb}_4{\rm S}_{13}$ ), chalcostibite (CuSbS $_2$ ), skinnerite (Cu $_3{\rm SbS}_3$ ), and famatinite (Cu $_3{\rm SbS}_4$ ).  $^{20}$  Famatinite features key properties that have a potential to benefit applications in solar cells and thermoelectric devices.

Famatinite has been classified as a superabsorber, featuring an optical absorption coefficient greater than 10<sup>4</sup> cm<sup>-1</sup> over the visible region.<sup>21,22</sup> The direct optical band gap of famatinite has been computationally determined to be 0.98 eV,<sup>23</sup> while

Received: June 23, 2022 Revised: September 17, 2022 Published: October 3, 2022





experimental results have shown indirect and direct band gaps ranging from 0.46 to 1.2 eV. 22,24-27 This range of values is likely due to differences in synthetic methods as well as the presence of structural defects or secondary phases.<sup>22</sup> Coupling the strong solar absorption coefficient and direct band gap with a high carrier mobility of 0.05-2 cm<sup>2</sup> V<sup>-1</sup> s<sup>-1</sup>, <sup>28</sup> famatinite has the potential to significantly impact solar cell technologies both as a hole transporter and as a light absorber. Initial efforts to produce thin films of famatinite as a p-type solar absorber incorporated famatinite by sputter deposition followed by thermal annealing. This produced solar conversion efficiencies of less than 1%, <sup>29,30</sup> which are postulated to be the result of elemental Cu and other CAS impurities produced by an annealing process.<sup>31</sup> Famatinite is conventionally synthesized by solid-state methods such as mechanical alloying coupled with either hot pressing or spark plasma sintering. 17,32-36 Nanoparticles have been synthesized using surfactant-mediated solvothermal and hot-injection routes, generally producing polycrystalline famatinite between 10 and 200 nm in size. 25,37-41

Famatinite has also been studied for its thermoelectric properties, as the bulk phase has been shown to possess a low lattice thermal conductivity ( $\kappa_{\rm L}$ ) and large Seebeck coefficient. Undoped famatinite has a reported ZT of 0.14 at 623 K, but researchers have utilized synthetic and doping strategies to improve famatinite ZT, with Sb-site doping being the most investigated strategy. A Bi and Sn co-doping strategy yielded a ZT of 0.76 at 623 K, while a Ge and P co-doping strategy resulted in a ZT of 0.67 at 673 K. The only demonstration of Cu-site dopant incorporation is Cu<sub>2</sub>ZnSbS<sub>4</sub>, which was produced by solid-state methods with secondary phases and did not undergo optical or thermal characterization. The pure-phase incorporation of Cu-site dopants remains an underexplored avenue toward the tuning of famatinite optical properties and thermoelectric properties.

Within the CAS phases, tetrahedrite is the most highly studied. Tetrahedrite and famatinite are closely related to each other, and direct conversion between famatinite to tetrahedrite has been observed. Tetrahedrite has shown great promise as a thermoelectric owing to its low thermal conductivity value of 0.5 Wm $^{-1}$  K $^{-1}$  when nanostructured,  $^{19,47-50}$  which stems from a complex unit cell and lattice anharmonicity from the Sb lone pairs. Doping with Zn to produce nanostructured Cu $_{11}$ ZnSb $_4$ S $_{13}$  (ZT = 1.09 at 723 K) further decreases the total thermal conductivity to 0.3 Wm $^{-1}$  K $^{-1}$  and is an example of a high-performing thermoelectric material synthesized by solution-phase methods.  $^{19,48}$  Chalcostibite and skinnerite are less studied but also attract interest for potential thermoelectric and photovoltaic applications.  $^{53-56}$ 

This research investigates the synthetic versatility of nanostructured famatinite and explores both its growth mechanism and thermal decomposition pathway. Using a solution-phase modified polyol method, synthesis of famatinite nanoparticles is demonstrated without ligands or surfactants. This solution-phase method is facile in its capacity to incorporate dopants and has produced phase-pure nanoparticles of Cu<sub>3-x</sub>M<sub>x</sub>SbS<sub>4</sub> (M = Ni, Zn, Mn, Fe) for the first time. Nanostructured materials enhance solar energy harvesting due to larger optical absorption coefficients and lower reflectivity<sup>57</sup> and improve the ZT of thermoelectric devices via increased phonon scattering originating from a greater number of grain boundaries and compositional inhomogeneities. The effects of ligand-free nanostructuring and Cu-site dopants on

the thermal and optical properties of famatinite were ascertained following synthetic optimization. Post-synthetic surface modification of famatinite nanoparticles was demonstrated, which can improve the solution-phase dispersibility of the nanoparticles and further tune material properties. Analysis of the structural, thermal, and optical properties of these new doped famatinite species was carried out by X-ray diffraction (XRD), scanning electron microscopy (SEM), transmission electron microscopy (TEM), energy-dispersive X-ray spectroscopy (EDS), thermogravimetric analysis (TGA), differential scanning calorimetry (DSC), and solid vis-NIR absorption spectroscopy. This study presents a solution-phase method for producing famatinite nanoparticles, shows the first pure-phase incorporation of Cu-site dopants, demonstrates the potential tunability of Cu-site dopants, characterizes the size of undoped and doped nanoparticles, quantifies the elemental composition of nanoparticles, determines the nature and size of the band gap of each Cu-site doped famatinite species, provides an indepth analysis of thermal stability that maps out compositional and structural changes as a function of annealing, and examines surface functionalization as a method to improve nanoparticle processability.

#### **■** EXPERIMENTAL SECTION

**Materials.** For the synthesis of undoped and doped famatinite nanoparticles,  $Cu(C_2H_3O_2)_2 \cdot H_2O$  (≥98%),  $Sb(C_2H_3O_2)_3$  (≥99.99%), sulfur powder (99.98%),  $Zn(C_2H_3O_2)_2$  (99.99%),  $Fe(C_2H_3O_2)_2$  (95%),  $Ni(C_2H_3O_2)_2$  (98%), and  $Mn(C_2H_3O_2)_2$  (98%) were procured from Aldrich Chemical Co. and used as received. Sodium borohydride (≥98%, Aldrich Chemical Co.) was used as a reducing agent in the synthesis. Tetraethylene glycol (99%, Alfa Aesar) was used as the primary solvent, and anhydrous ethanol (200 proof, USP grade, Pharmco-Aaper) was used to isolate the final product. 1-Octadecanethiol (ODT) (≥97.5%, Fluka Analytical), 11-mercapto-1-undecanol (MUD) (97%, Aldrich Chemical Co.), and n-hexane (95%, Pharmco-Aaper) were used to investigate post-synthetic surface functionalization of nanoparticles.

Synthetic Procedure. A typical reaction for Cu<sub>3</sub>SbS<sub>4</sub> produced approximately 440 mg (1.0 mmol) of nanostructured materials from a one-pot reaction. Reagents were added into a 250 mL round-bottom flask in the following stoichiometric ratios:  $Cu(C_2H_3O_2)_2 \cdot H_2O$  (0.60 g, 3.0 mmol), Sb(C<sub>2</sub>H<sub>3</sub>O<sub>2</sub>)<sub>3</sub> (0.30 g, 1.0 mmol), and sulfur powder (0.13 g, 4.0 mmol). These precursors were subsequently dissolved in 30 mL of tetraethylene glycol, yielding a blue coloration. The resulting mixture was stirred and sparged with N2 gas. Approximately 0.60 g (15 mmol) of sodium borohydride was dispersed in 20 mL of tetraethylene glycol, sonicated, and then slowly added to the roundbottom flask upon the completion of sparging. Following the introduction of sodium borohydride, the temperature increased, and reduction was observed to begin as the solution became darkly colored. Under nitrogen flow, the reaction was heated to 175 °C, held for 1 h, and then allowed to cool to room temperature. The resulting mixture was loaded into centrifuge tubes and centrifuged at 4000 rpm for 10 min. This was followed by removal of the supernatant, a wash of the remaining pellet with anhydrous ethanol, sonication, and another round of centrifugation. This process was repeated four times, with the final product left to dry overnight in a vacuum desiccator. The resulting Cu<sub>3</sub>SbS<sub>4</sub> powder samples appeared black. All products were characterized by XRD and SEM with EDS to confirm phase purity and determine elemental composition.

In a reaction to produce Cu-site doped Cu<sub>3</sub>SbS<sub>4</sub>, the same steps were followed with slight variations. For each synthesis, an additional 0.40 mmol (10% excess) of sulfur powder was added. Each dopant was added in at a stoichiometric ratio corresponding to the desired dopant concentration, while the amount of copper precursor was decreased by the same amount. Cu<sub>3-x</sub>M<sub>x</sub>SbS<sub>4</sub> (M = Zn, Ni, Mn, Fe) were all synthesized with added sulfur in the reaction. All resulting

powders appeared black, apart from  $\text{Cu}_2\text{ZnSbS}_4$ , which possessed a uniform slightly red tinge. Sb- and S-site dopants were produced using this same synthetic methodology with 10% mol excess sulfur incorporation. Undoped famatinite synthesized with 0% mol excess S is identified as  $\text{Cu}_3\text{SbS}_4$  (1), and undoped famatinite with 10% mol excess S is identified as  $\text{Cu}_3\text{SbS}_4$  (2).

To optimize the synthesis and better understand the reaction pathway, the polyol synthesis of famatinite was performed and characterized as a function of temperature and time. For the temperature-based study, nanoparticles were synthesized and washed as indicated above, with the reaction temperature varied from 100 to 200  $^{\circ}\mathrm{C}$  and held for 1 h. To optimize the reaction time at this temperature, the hold-time of the synthesis was varied between 0 and 90 min. Characterization by SEM, EDS, and XRD was conducted. The temperature and time studies identified the optimal time and temperature to be 60 min at 175  $^{\circ}\mathrm{C}$ .

Post-synthetic surface modification of famatinite nanoparticles was undertaken using alkanethiols. The hydroxyl-terminated alkanethiol (MUD) and the methyl-terminated alkanethiol (ODT) were employed to impart the nanoparticles with hydrophilic and hydrophobic surface properties, respectively. To prepare 100 mL of 5.0 mM ethanolic solution, 0.10 g (0.50 mmol) of MUD or 0.15 g (0.50 mmol) of ODT was massed and dissolved. Subsequently, 50 mg (0.1 mmol) of Cu<sub>3</sub>SbS<sub>4</sub> was massed and placed in 10 mL of the 5 mM alkanethiol solution. This mixture was sonicated for 20 min. To remove the solvent and excess ligand, the mixture was loaded into microcentrifuge tubes and centrifuged at 13,000 rpm for 10 min, with the supernatant discarded and the solid retained at the end of each centrifugation. This process was repeated four times with consolidation of the pellets. The final pellet was kept overnight under vacuum desiccation. A control was also made using the same process, but no ligand was introduced. To test nanoparticle dispersibility, 2 mg of either functionalized nanoparticles or control nanoparticles was placed into a glass vial that was then filled with 15 mL of anhydrous ethanol, deionized water, or n-hexane. Photos were taken across 32 days to assess the impact of the ligand functionalization on solutionphase stability of the nanoparticles. These functionalized particles were not characterized by optical spectroscopy or thermal analysis.

**Characterization Methods.** The structure and composition of the famatinite nanoparticles were investigated by XRD, SEM, EDS, and TEM. The thermal properties were investigated by DSC and TGA, and the optical properties were studied by solid vis—NIR absorption spectroscopy.

Powder XRD patterns were obtained by a Rigaku Miniflex II benchtop diffractometer over a  $2\theta$  of  $10-70^\circ$  via Cu K $\alpha$  radiation of 30 kV and 15 mA. Pattern collection was completed with a scan speed of  $3^\circ$  per min and a sampling width of  $0.03^\circ$ . Rietveld refinements on each pattern were undertaken utilizing the PDXL2 analysis software to calculate lattice constants, crystallite size, and crystallite strain. Famatinite<sup>59</sup> (Cu<sub>3</sub>SbS<sub>4</sub>) PDF#01-071-0555, tetrahedrite<sup>60</sup> (Cu<sub>12</sub>Sb<sub>4</sub>S<sub>13</sub>) PDF#01-074-0270, covellite<sup>61</sup> (CuS) PDF#03-065-3928, and valentinite<sup>62</sup> (Sb<sub>2</sub>O<sub>3</sub>) PDF#00-001-0729 reference patterns were utilized in data analysis.

SEM images and EDS spectra were gathered using a JEOL JSM IT-200LA equipped with a JEOL JED-2300 Dry SDD EDS detector. An accelerating voltage of 15 keV was used to acquire the images and spectra, with each sample characterized at a minimum of three locations to affirm sample homogeneity. Averages and standard deviations were obtained from these multiple locations and are reported throughout. Samples were prepared by adhering nanoparticle samples to a carbon tape and placing in a vacuum chamber for at least 1 h prior to analysis.

TEM images were taken using an FEI Talos F200X with an accelerating voltage of 200 keV. Each sample was prepared for analysis by placing the nanoparticles in ethanol, sonicating, and subsequently drop-casting the solution onto lacey carbon coated TEM grids.

The thermal properties of the as-synthesized famatinite nanoparticles were investigated by TGA and DSC. TGA analysis was performed from 25 to 700 °C using a TA TGA Q500. Approximately 10 mg of the material was heated under nitrogen flow in an alumina ceramic pan at a heating rate of  $10~^{\circ}\text{C}$  min $^{-1}$  and a sampling time of 2.00 s per point. Results were replicated to confirm the reproducibility of the result. DSC analysis was performed from 50 to 550  $^{\circ}\text{C}$  using a TA DSC Q2000. Approximately 10 mg of the material was placed in a graphite pan with a graphite lid. The heating rate was  $10~^{\circ}\text{C}$  min $^{-1}$  with a sampling time of 0.20 s per point. DSC characterization was replicated to confirm the reproducibility of the phase transitions.

The optical properties of the famatinite nanoparticles were investigated by vis-IR spectroscopy. Spectra were collected using a Perkin-Elmer Lambda 950 spectrometer featuring an integrating sphere with PMT and InGaAs detectors. Solid samples were drop-cast from ethanol, sandwiched between NIR-transparent quartz plates (Spectrocell, Oreland, PA), and analyzed at the reflectance port of the integrating sphere. Spectra were collected in the range of 2200 to 300 nm in 1 nm increments. Detector response settings were 0.40 s. The InGaAs detector gain was 15 with a servo-controlled slit width. The PMT detector used autogain and a 1.5 nm slit width. Prior to sample measurement, the instrument was auto-zeroed with sandwiched quartz plates in front of a Spectralon reference. Spectral analysis was carried out with the Origin 9.1 software. Band gaps were assessed using Tauc plots in which normalized absorbance (A) was used because the thickness (t) of the drop-cast samples and thus the absorptivity ( $\alpha$ ) were unknown. The relationship between absorbance, film thickness, and absorptivity is described by  $A = t \times 2.303 \times 10^{-5}$  $\alpha$ . Substituting normalized absorbance for absorptivity affects the magnitude of the slope and does not impact the linearity and xintercept, which are utilized to identify if the band gap is indirect or direct and to determine the magnitude of the band gap, respectively. Optical characterization by Raman spectroscopy was also conducted (details in the Supporting Information (SI)).

**Thermal Analysis Methods.** The thermal stability and decomposition pathway of  $Cu_3SbS_4$  and  $Cu_{3-x}M_xSbS_4$  (M=Zn, Ni, Mn, Fe) were investigated to identify the source of TGA mass loss and DSC phase changes. Samples of each powder (10 mg) were annealed to a temperature of 100, 200, 300, 400, or 500 °C at a rate of 10~ °C min $^{-1}$  while under continuous nitrogen flow. After the annealing temperature was achieved, heating ceased, and the powder returned to room temperature under nitrogen flow. XRD, SEM, and EDS were performed on each product to determine structural and compositional changes that occurred during the annealing process.

#### ■ RESULTS AND DISCUSSION

The reaction pathway for famatinite was studied by XRD, SEM, EDS, and TEM to determine optimal synthetic parameters and key intermediates. Dopants were incorporated into the lattice to tune the optical properties and alter thermal stability. Optical studies were conducted on each doped species using vis—NIR absorption spectroscopy to determine the nature and size of the band gap. TGA, DSC, XRD, and EDS results were gathered in a systematic thermal analysis study that investigated the mass loss, phase transitions, structural properties, and elemental composition as a function of temperature. To improve the processability of famatinite nanoparticles, post-synthetic surface functionalization studies were completed. The synthetic versatility of the modified polyol process and the effects of nanostructuring and dopant incorporation on optical and thermal properties are presented herein.

Synthetic Optimization and Characterization of Famatinite. Famatinite was previously observed as a growth mechanism intermediate in the modified polyol process developed to produce nanoparticles of tetrahedrite  $(Cu_{12}Sb_4S_{13})$ . Herein, the reaction pathway for famatinite was investigated as a function of temperature and time. To determine the optimal synthetic parameters of famatinite synthesis, the reaction temperature was varied between 100 and 200 °C, holding for 1 h, then the phases present were

characterized by XRD and EDS (Figure 1 and Table S1). At 100 °C, the products were primarily amorphous, but by 125

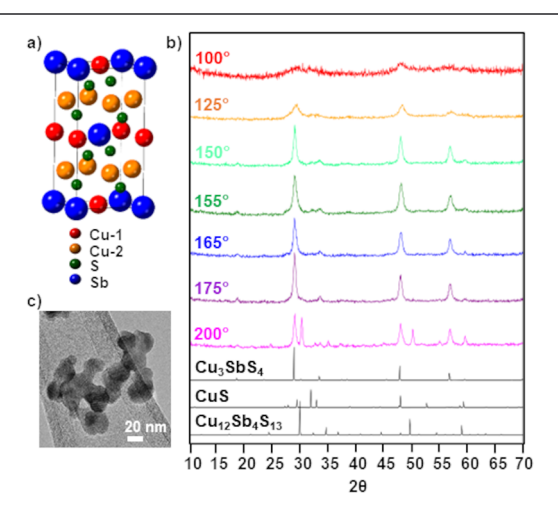


**Figure 1.** (a) The unit cell of famatinite is tetragonal with the space group I42m. <sup>59</sup> (b) XRD patterns of samples produced after reacting at the indicated temperature for 1 h.  $Cu_3SbS_4$  (#01-071-0555), <sup>59</sup> CuS (#03-065-3928), <sup>61</sup> and  $Cu_{12}Sb_4S_{13}$  (#01-074-0270) <sup>60</sup> provided as reference patterns. (c) Representative TEM image of  $Cu_3SbS_4$  nanoparticles.

°C, famatinite was formed as a primary phase alongside a secondary phase of covellite (CuS). At 150 and 155 °C, covellite persisted as a minor secondary phase with its most intense peak (at ~32°) significantly decreased and broadened at 165 °C. By XRD, this covellite peak was eliminated at 175 °C, although thermal analysis and Raman data suggest that slight impurities may remain (described in the Thermal Analysis section). By EDS (Table S1), the average elemental ratio of antimony increased from a deficiency of  $0.88 \pm 0.01$  at 125 °C to a slight excess of 1.098  $\pm$  0.005 at 175 °C, which further supports the conclusion that the secondary covellite phase is no longer detectable at 175 °C. Considering both the elemental analysis and crystalline purity, the product synthesized at 175 °C was closest to the desired famatinite target ratio, with an elemental composition determined by EDS to be  $Cu_{3.32\pm0.03}Sb_{1.098\pm0.005}S_{4.00\pm0.03}$ . At 200 °C, tetrahedrite (Cu<sub>12</sub>Sb<sub>4</sub>S<sub>13</sub>) emerged as a significant phase, with EDS corroborating this conclusion by a decrease in sulfur ratio (Table S1). Tetrahedrite and famatinite are known to be interconvertible phases, and the change from famatinite to tetrahedrite at high temperatures is consistent with previous studies.22,46

With EDS and XRD results suggesting 175 °C to be the best reaction temperature to obtain phase-pure Cu<sub>3</sub>SbS<sub>4</sub>, a time-based study at 175 °C was conducted where the hold time of the reaction was varied (Figure S1 and Table S2). At 0 and 15 min, phases of famatinite, covellite, and valentinite (Sb<sub>2</sub>O<sub>3</sub>) were all observed. From 30 to 90 min, famatinite is the only product observed by XRD. EDS results (Table S2) indicate that, at 30 min, the product is 20% Cu enriched and 5% Sb enriched. At 60 min, the result is 10% Cu enriched and 10% Sb enriched, while the 90 min result is 20% Cu enriched and 20% Sb enriched. Thus, the product formed at 60 min was selected as the most favorable reaction time. This elemental analysis supports the hypothesis that CuS and Sb are the key drivers of famatinite formation. At the hold time of 0 min, the product is Sb deficient because the Sb in the reaction has not had

sufficient time to fully reduce and react; therefore, it was removed with the supernatant in the wash process. The presence of  $\mathrm{Sb_2O_3}$  at 15 min is an indicator that reduced Sb is available for the reaction but has not yet fully incorporated with CuS. The  $\mathrm{Sb_2O_3}$  impurity observed at this time is likely formed by the reaction of elemental Sb with oxygen during the centrifugation wash process postsynthesis. The limiting step of the reaction is hypothesized to be the reduction of Sb that then reacts with covellite in the presence of excess S to form famatinite.

While exploration of reaction time and temperature identified that phase-pure famatinite was obtained with reactions for 60 min at 175 °C, the relative copper and antimony excess led to additional attempts to improve the phase purity of famatinite. The effect of sulfur addition to the reaction mixture was examined. An excess of 10% mol S was added to the synthesis, which is consistent with other synthetic approaches that used excess sulfur during an anneal of their product under sulfur vapor to improve phase purity and elemental composition. <sup>29,31,63</sup> The result was pure-phase famatinite by XRD (Figure 2) with an average elemental

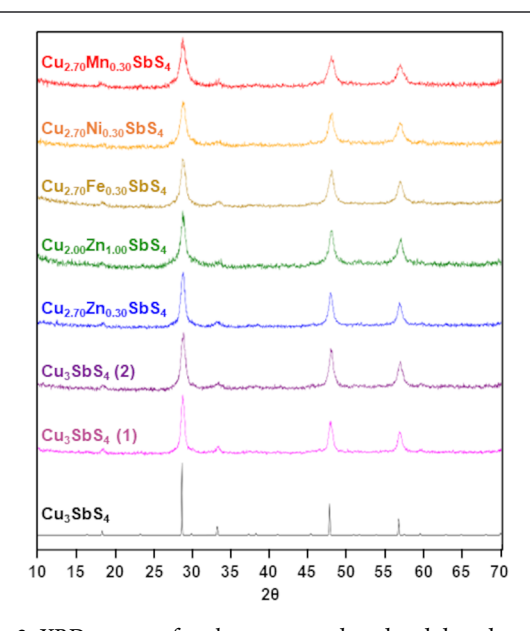


**Figure 2.** XRD patterns for phase-pure undoped and doped species of famatinite along with the reference famatinite pattern (#01-071-0555).  $^{59}$  Cu<sub>3</sub>SbS<sub>4</sub> (1) and Cu<sub>3</sub>SbS<sub>4</sub> (2) represent 0 and 10% additional sulfur in the reaction, respectively.

ratio by EDS of  $Cu_{3.10\pm0.02}Sb_{1.04\pm0.01}S_{4.00\pm0.02}$  (referred to as  $Cu_3SbS_4$  (2)). This is an improvement over the composition obtained at the optimal conditions without the additional sulfur, which possessed an average elemental ratio by EDS of  $Cu_{3.32\pm0.03}Sb_{1.098\pm0.005}S_{4.00\pm0.03}$  (referred to as  $Cu_3SbS_4$  (1)). This 10% mol excess resulted in an enrichment of less than 5% for Cu and Sb, which is more than half the enrichment observed without excess sulfur. The famatinite stoichiometry reported herein of  $Cu_{3.10\pm0.02}Sb_{1.04\pm0.01}S_{4.00\pm0.02}$  has excellent fidelity relative to the target composition when compared to compounds in the literature values that have ratios from  $Cu_{2.50}Sb_{1.45}S_{4.00}$  (16% Cu deficient) to  $Cu_{4.44}Sb_{1.31}S_{4.00}$  (48% Cu enriched) and are phase-pure by XRD.  $Cu_{17,34,43,64}$ 

The morphology and size of  $Cu_3SbS_4$  (2) nanoparticles were characterized by TEM and analyzed by Rietveld refinements of XRD patterns. Nanoparticles were shown to be heterogeneous

Table 1. Elemental Analysis of Famatinite Compounds as Determined by EDS, with Average Atomic Ratios and Standard Deviations Provided<sup>a</sup>

atomic ratios determined by EDS				
target	Cu	dopant	Sb	S
$Cu_{2.70}Mn_{0.30}SbS_4$	$2.91 \pm 0.06$	$0.295 \pm 0.005$	$1.066 \pm 0.007$	$4.00 \pm 0.7$
$\mathrm{Cu_{2.70}Ni_{0.30}SbS_4}$	$2.88 \pm 0.04$	$0.25 \pm 0.03$	$1.08 \pm 0.01$	$4.00 \pm 0.3$
$Cu_{2.70}Fe_{0.30}SbS_4$	$2.84 \pm 0.01$	$0.250 \pm 0.008$	$0.97 \pm 0.01$	$4.00 \pm 0.2$
$Cu_{2.00}Zn_{1.00}SbS_4$	$2.09 \pm 0.06$	$0.96 \pm 0.04$	$0.96 \pm 0.01$	$4.00 \pm 0.7$
$Cu_{2.70}Zn_{0.30}SbS_4$	$2.80 \pm 0.03$	$0.32 \pm 0.01$	$1.044 \pm 0.007$	$4.00 \pm 0.2$
$Cu_3SbS_4$ (2)	$3.10 \pm 0.02$		$1.04 \pm 0.01$	$4.00 \pm 0.2$
$Cu_3SbS_4$ (1)	$3.32 \pm 0.03$		$1.098 \pm 0.005$	$4.00 \pm 0.3$

<sup>&</sup>quot;Atomic ratios are determined by normalizing S to 4. Cu<sub>3</sub>SbS<sub>4</sub> (1) and Cu<sub>3</sub>SbS<sub>4</sub> (2) represent 0 and 10% additional sulfur in the reaction, respectively.

in size and shape, ranging from 20 to 30 nm in size (Figure 1c and Figure S2). This variability is anticipated because the synthetic method is surfactant- and ligand-free. Ligand-free nanoparticles are advantageous for thermoelectric applications because ligand shells decrease electrical conductivity. As described later, these particles can be post-synthetically modified with selected ligands to tune solubility and other material properties.  $\text{Cu}_3\text{SbS}_4$  (2) nanoparticles are polycrystalline with Rietveld refinements showing individual crystallites ranging between 8 and 11 nm (Table S3).

Dopant Incorporation. Prior approaches to doping famatinite have primarily focused on the Sb-site and used solid-state fabrication methods. 17,32,33,66 Utilizing the optimized synthesis developed here, famatinite was shown to integrate Mn, Ni, Fe, and Zn as dopants on the Cu-site. All Cusite-doped materials are single-phase by XRD (Figure 2) and possess elemental ratios determined by EDS that adhere closely to the target stoichiometry (Table 1). With the addition of dopants, the proximity to the target chemical formula was maintained with the sum of the Cu and the Cu-dopant in the atomic ratio revealing an enrichment above the target between 2 and 7%, which is consistent with what was found for the optimized undoped famatinite. The calculated standard deviations for the chemical formulas determined by collecting EDS data at multiple sample locations were small (typically less than 2% relative standard deviation), indicating a high degree of homogeneity throughout the sample. TEM images of doped samples are similar in the general size and shape of the nanoparticles in comparison to the undoped samples with a diameter of ~20 nm (Figure S2). XRD Rietveld refinements show that the individual crystallite size of doped samples ranged from 4 to 9 nm in comparison to undoped samples that ranged from 8 to 11 nm in size (Table S3).

This study marks the first time Mn or Fe has ever been incorporated into famatinite, and it is the first time incorporating Zn and Ni phase-pure. Doping of  $\mathrm{Cu_{3-x}Zn_xSbS_4}$  with stoichiometries ranging from x=0.3 to 1.0 represents the first demonstration that Cu-site dopants are tunable. The Zn dopant was selected for this tunability study because it had been shown for the related compound of tetrahedrite that Zn doping resulted in the largest ZT. <sup>19,48</sup> Other dopants were successfully incorporated, including Ag on the Cu-site; In, Bi, and Sn on the Sb-site; as well as Se on the S-site (Figure S3 and Table S4). This is the first demonstration of Ag and In doping into famatinite.

**Thermal Stability.** For photovoltaic and thermoelectric applications, it is important to evaluate the thermal stability of a material due to its proximity to moderate or high heat during

device usage. Some previous TGA and DSC studies have investigated famatinite synthesized by traditional solid-state methods, <sup>17,32,33,43</sup> but this is the first thermal analysis of famatinite nanoparticles made by solution-phase methods and the first to look at famatinite with Cu-site dopants. To accompany TGA and DSC analysis, samples were annealed systematically, and products were studied by XRD, SEM, and EDS as an in-depth study of the annealing process and decomposition products.

As-synthesized famatinite nanoparticles with and without Cu-site dopants were subjected to thermal analysis by TGA and DSC (Figure 3 and Figures S4-S5). Cu<sub>3</sub>SbS<sub>4</sub> (1) and Cu<sub>3</sub>SbS<sub>4</sub> (2) had similar thermal decomposition TGA traces (Figure 3a and Figure S4), indicating that the excess amount of sulfur added for the reaction of Cu<sub>3</sub>SbS<sub>4</sub> (2) did not alter the thermal stability of the nanoparticles. Both samples lost approximately 17% of their total starting mass by 700 °C. The undoped samples are best characterized by their prolonged continuous mass loss from 200 to 440 °C, but the mass of the sample is then steady to 700 °C. This type of mass loss is shared by the Ni- and Fe-doped species, with Cu<sub>2,70</sub>Ni<sub>0,30</sub>SbS<sub>4</sub> losing 17% by 700 °C and Cu<sub>2,70</sub>Fe<sub>0,30</sub>SbS<sub>4</sub> losing 21% by 700 °C. The  $Cu_{2.70}Zn_{0.30}SbS_4$  sample does not share the same continuous mass loss feature from 200 to 440 °C, but instead displays the greatest thermal stability up to 350 °C with a mass loss of only 4%. Above 350 °C, there is then a steady mass loss that ends approximately equal to Cu<sub>2</sub>ZnSbS<sub>4</sub> by 500 °C. Cu<sub>2.70</sub>Zn<sub>0.30</sub>SbS<sub>4</sub> and Cu<sub>2</sub>ZnSbS<sub>4</sub> have the smallest mass loss overall of 10% at 700 °C. However, Cu<sub>2</sub>ZnSbS<sub>4</sub> has a slow mass loss of 2 to 8% from 200 to 440 °C unlike  $\text{Cu}_{2.70}\text{Zn}_{0.30}\text{SbS}_4$  ,  $\text{Cu}_{2.70}\text{Mn}_{0.30}\text{SbS}_4$  has little mass loss from 200 to 440 °C, and by 440 °C, it has the smallest overall mass loss of 6%. A significant mass loss then begins at around 500 °C, and at 700 °C, there is a total mass loss of 13%. All samples displayed a small mass loss of 1-3% at low temperatures (50-250 °C), which could stem from residual polyol solvent.

Both undoped famatinite samples have the same transitions by DSC and have more observed phase transitions than all doped famatinite species (Figure 3b and Figure S5). A potential reason for the number of transitions that occurs in the undoped samples is the presence of a small amorphous CuS impurity detected by Raman spectroscopy, as shown in Figure S6. The largest transition is endothermic at 400  $^{\circ}$ C, and all undoped as well as doped famatinite samples have a transition at or near this temperature, although the magnitude varies. Cu<sub>2.70</sub>Fe<sub>0.30</sub>SbS<sub>4</sub> has the largest mass loss by TGA and has more DSC transitions than the other doped samples. Cu<sub>2.70</sub>Ni<sub>0.30</sub>SbS<sub>4</sub> shares a similar intensity in its 400  $^{\circ}$ C

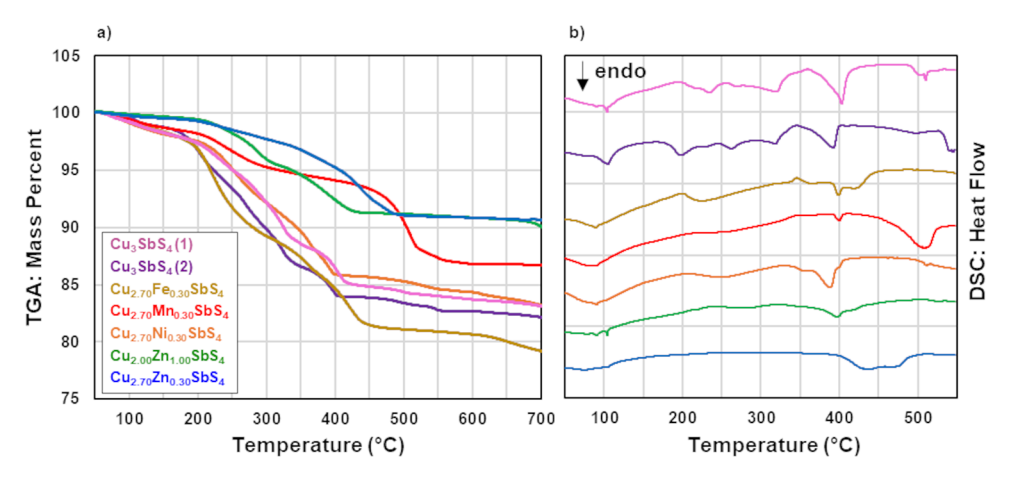


**Figure 3.** Thermal analysis of undoped and doped famatinite samples by (a) TGA and (b) DSC. Legend corresponds to both graphics.  $Cu_3SbS_4$  (1) and  $Cu_3SbS_4$  (2) represent 0 and 10% additional sulfur in the reaction, respectively. DSC curves are stacked for clarity, and each increment on the y axis is 0.5 W/g.

transition to the undoped famatinite species, but it occurs at a slightly lower temperature. Both Zn-doped samples have results that show stability from 100 to 400 °C with minimal phase changes in contrast to the undoped, Ni-doped, and Fedoped samples. Cu<sub>2</sub>ZnSbS<sub>4</sub> has a small endothermic transition at approximately 400 °C as most other samples do, but it is broader and less intense. In contrast, the transition in Cu<sub>2.70</sub>Zn<sub>0.30</sub>SbS<sub>4</sub> is shifted to a slightly higher temperature and appears to be composed of two broad features over the range of 425 to 475 °C. Cu<sub>2.70</sub>Mn<sub>0.30</sub>SbS<sub>4</sub> has a small 400 °C endothermic transition with a major endothermic transition that occurs at 500 °C and is not shared by any other species. Considering the DSC and TGA results, it is concluded that doping famatinite with Zn and Mn improves the thermal stability of the nanoparticles by decreasing the amount of mass lost and reducing the number of phase transitions.

For famatinite ( $Cu_3SbS_4$  and  $Cu_3Sb_{0.92}M_{0.08}S_4$ , M = Sn, Ge) made by mechanical alloying with hot pressing at 300 °C, mass loss by TGA of approximately 8-10% was observed after heating to 700 °C. 17,33,43 Additionally, for these samples, two endothermic DSC transitions were observed between 530 and 615 °C in all cases. 17,33,43 For the famatinite samples produced by the polyol method herein, this mass loss is greater for all samples (13-21%) relative to the solid-state precedent, with the exception of Zn-doped famatinite samples (10%). All samples made by the modified polyol method had an endothermic transition at the lower temperature of ~400 °C. The solution-phase method utilized in this study produced nanoparticles, which are likely the cause of the decreased thermal stability. One study that produced famatinite  $(Cu_3Sb_{0.89}Bi_{0.06}Sn_{0.05}S_4)$  by mechanical alloying and spark plasma sintering at 400 °C produced particles of around 100 nm in size.<sup>32</sup> TGA and DSC of this material are very comparable to those of the famatinite made by the modified polyol method, with a TGA mass loss of around 10% by 475 °C and an endothermic DSC transition at 438 °C. The aforementioned solid-state methods employed an annealing process prior to characterization that likely eliminated the low temperature (50–300 °C) DSC transitions and TGA mass loss that were observed for most of the as-synthesized polyol samples.

To investigate the composition and structure of famatinite in parallel with the thermal properties revealed by DSC and TGA, XRD, SEM, and EDS characterization was undertaken for the species produced by annealing under nitrogen gas at set heating intervals (100 °C from 100 to 500 °C). XRD results for the samples annealed at 100 and 200 °C were consistent with those of the as-synthesized products and the 300 °C products (Figure S7). At 300 °C, all products remain phasepure by XRD (Figure 4a) despite the mass losses ranging from 2.5 to 11% observed in the TGA (Figure 3a). This shows that the famatinite nanoparticles made by the modified polyol can be annealed to 300 °C, which will likely further stabilize the phase for thermoelectric or solar cell applications. By 400 °C, all XRD patterns (Figure 4a) reveal crystalline decomposition products (primarily tetrahedrite). This observation of a new phase correlates with the endothermic transition that occurred at approximately 400 °C for all samples by DSC. This finding is consistent with the ease of transformation between famatinite and tetrahedrite phases reported in prior literature. 22,46,47 Tetrahedrite is the primary phase after heating to 400 °C for all samples except Cu<sub>2.70</sub>Mn<sub>0.30</sub>SbS<sub>4</sub> and Cu<sub>2.70</sub>Zn<sub>0.30</sub>SbS<sub>4</sub> (Figure 4a), which suggests that doping stabilized famatinite and results in the transformation between phases. In both of the aforementioned samples, famatinite is still observed as a dominant phase. At 500 °C, famatinite is still present in the Cu<sub>2,70</sub>Mn<sub>0,30</sub>SbS<sub>4</sub> sample as a secondary phase, while all other doped famatinite species have been converted to tetrahedrite phases (Figure 4a). At 400 and 500 °C for Cu<sub>2</sub>ZnSbS<sub>4</sub> and Cu<sub>2.70</sub>Zn<sub>0.30</sub>SbS<sub>4</sub>, respectively, a color change from black to brick red occurs. This supports the XRD finding that tetrahedrite has formed based on prior research that reported the red color of  $Cu_{10}Zn_2Sb_4S_{13}$  and  $Cu_{11}ZnSb_4S_{13}$ . In both undoped species, a color change to gray is observed after heating to 500 °C, and a second tetrahedrite phase is observed by XRD that represents a copper-rich tetrahedrite phase as previously reported.<sup>67</sup> Consistent with TGA data, XRD results demonstrate that Cu<sub>2.70</sub>Mn<sub>0.30</sub>SbS<sub>4</sub> and Cu<sub>2.70</sub>Zn<sub>0.30</sub>SbS<sub>4</sub> possess phase stability that is greater than that of the undoped and other doped species.

To investigate by EDS the compositional change upon heating, the atomic percent after annealing is subtracted from the atomic percent of the as-synthesized product (atomic percentages provided in Table S5). For the EDS data graphed in Figure 4b, this change in the atomic percent is graphed relative to the annealing temperature. The undoped samples

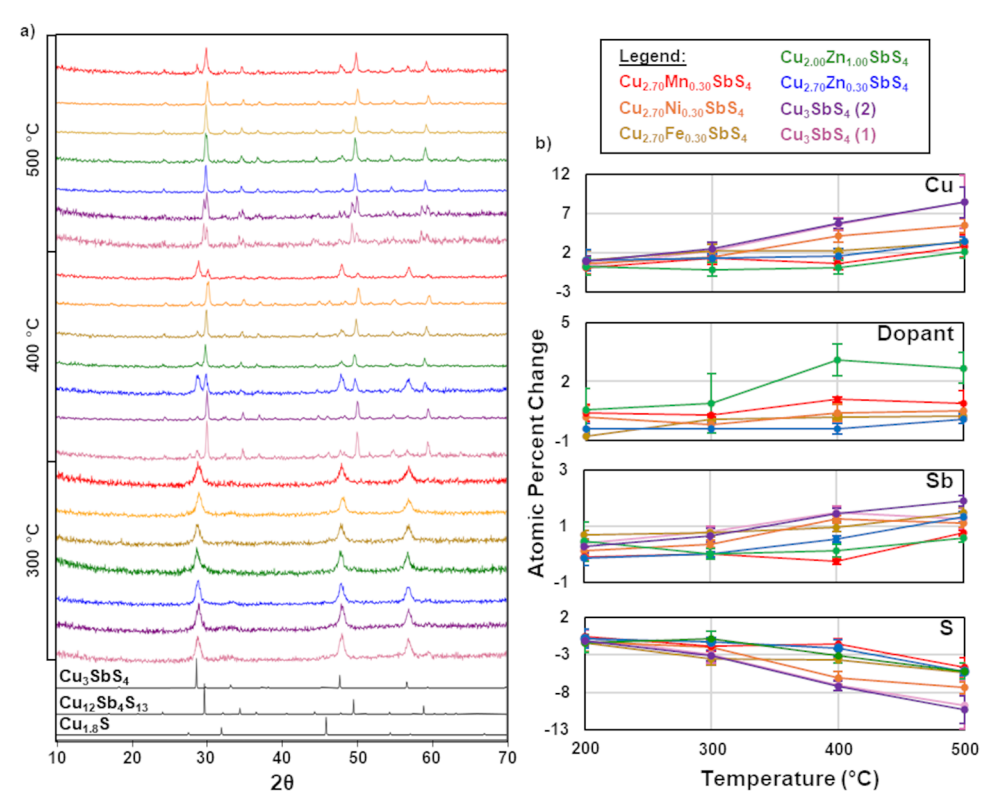


Figure 4. (a) XRD of undoped and doped famatinite samples after annealing to 300, 400, and 500 °C. References for  $Cu_3SbS_4$  (01-071-0555),  $^{59}$   $Cu_{12}Sb_4S_{13}$  (01-074-0270),  $^{60}$  and  $Cu_{1.8}S$  (01-085-1693)  $^{68}$  provided. (b) Change in EDS atomic percentage, with error, plotted as a function of temperature for the undoped and doped famatinite samples. In all cases, the atomic percent determined after annealing is compared to the atomic percent of the synthetic product to determine the atomic percent change.  $Cu_3SbS_4$  (1) and  $Cu_3SbS_4$  (2) represent 0 and 10% additional sulfur in the reaction.

lose S at a much greater rate than any of the other samples. In comparison to Mn and Zn dopants, this S loss is nearly doubled. For the Fe- and Ni-doped samples that possessed similar TGA mass loss to the undoped, the sulfur loss is less than the undoped samples and more than the Mn- and Zn-doped samples. The conversion from famatinite to tetrahedrite observed by XRD is directly linked to sulfur loss, and samples with the lowest sulfur loss displayed the greatest famatinite stability by XRD. The increase in the atomic percentage of Cu, Sb, and the dopant is inversely linked to the sulfur loss. Note that  $\text{Cu}_2\text{ZnSbS}_4$  has a greater increase in the dopant percentage from the as-synthesized number because it contains a greater absolute atomic percentage of the dopant relative to the other  $\text{Cu}_{2.70}\text{M}_{0.30}\text{SbS}_{4.00}$  compositions.

For the decomposition analysis by XRD and EDS, it was shown that the retention of sulfur correlates with the phase stability of famatinite. The stronger bonding character between each transition metal tetrahedrally coordinated to four S atoms in the lattice would inhibit S volatilization. The improvement in the thermal stability of the Mn- and Zn-doped samples likely stems from the strength of their sulfur interaction. For the initial interrogation of this observation, melting points of binary sulfides are here compared as a substitute for bond strength. MnS and ZnS have the highest melting points at 1610 and 1850 °C, whereas NiS, CuS, and FeS have lower melting points of 797, 500, and 1194 °C.69-73 Relatedly, it is notable that the MnS phase diagram is less complex than the phase diagrams of CuS and FeS in particular.<sup>74</sup> Additionally, the thermal stabilities observed for Cu-doped famatinites are consistent with those previously observed for Cu-doped

tetrahedrites. Zn-doped tetrahedrite was found to have the largest shift in the phase transition temperature observed by DSC, and Mn-doped tetrahedrite was found to have the least mass loss by TGA.<sup>75,76</sup> As Cu-site dopants on these CAS phases (famatinite and tetrahedrite) have been shown to improve thermal stability and tune material properties, <sup>75,76</sup> further research using electron pair resonance and X-ray photoelectron spectroscopy is planned to better understand bonding characteristics within the structure.

Optical Properties. The solution-phase synthesis here produces famatinite samples with direct band gaps that are little altered by Cu-site doping. The normalized vis-NIR absorbance spectra for undoped and doped famatinite are given in Figure 5a. All absorption curves for famatinite have similar slopes, with the undoped samples having the steepest change at approximately 1300 nm. These absorption spectra are converted into Tauc plots as shown in Figure 5b and Figure S8. Comparing the plots of  $(Ah\nu)^{1/2}$  (Figure S8) and  $(Ah\nu^2)$  (Figure 5b) versus photon energy shows that the plot  $(Ah\nu^2)$  yields good linear fits unlike  $(Ah\nu)^{1/2}$ . This indicates that the band gap is predominantly direct; if  $(Ah\nu)^{1/2}$  were linear, the band gap would be indirect. The lack of linearity demonstrated in the indirect plotting of the result coupled with the high linearity of the direct band gap result is evidence that the undoped and doped famatinite nanoparticles synthesized by the modified polyol method have a direct band gap.

In the literature, a variety of synthetic strategies have produced famatinite, but the nature of the band gap has varied between direct and indirect (Table S6). 15,22,24-26,28-32,35-37,39,40,46,63,64,66,78-85 For solution-

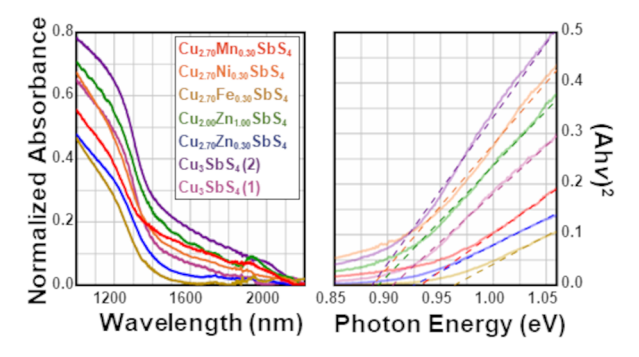


**Figure 5.** Normalized absorption spectra (left) and associated Tauc plot (right) of undoped and doped famatinite samples. Tauc plot contains photon energy (eV) versus  $(Ah\nu)^2$ , where A represents normalized absorbance, and reveals a linear relationship indicative of a direct band gap. Dashed lines represent linear fits for the data and indicate the x-intercept. Legend corresponds to both graphics.  $Cu_3SbS_4$  (1) and  $Cu_3SbS_4$  (2) represent 0 and 10% excess sulfur in the reaction, respectively.

phase methods that produce materials with indirect band gaps, annealing has been identified as a remedy to shift the dominant mode of charge excitation to be direct.<sup>22</sup> All famatinite nanoparticles produced herein by this solution-phase, surfactant-free modified polyol method possessed a direct band gap without the need for an annealing step.

To investigate the band gaps of doped and undoped samples, the x-intercepts of the best-fit-line through  $(Ah\nu)^2$ were compared. Band gaps of each famatinite species ranged from 0.85 to 0.95 eV, with each dashed line plotting the linear region of each dopant back to the x-intercept (Figure 5b). These values are in line with the reported literature based on computational and experimental findings. 22,24-27 The band gap of Cu<sub>3</sub>SbS<sub>4</sub> (1) was approximately 0.91 eV, while the band gap of Cu<sub>3</sub>SbS<sub>4</sub> (2) was around 0.87 eV. Cu<sub>2.70</sub>Fe<sub>0.30</sub>SbS<sub>4</sub>,  $Cu_{2.70}Zn_{0.30}SbS_4$ , and  $Cu_{2.70}Mn_{0.30}SbS_4$  all have band gaps higher than either undoped famatinite. All other dopants were found to be in-between the values of the undoped famatinites. These doped famatinite samples, which displayed improved thermal stability, maintained similar band gap properties to the undoped with some being slightly blue shifted, which is more favorable for photovoltaic applications. This is in contrast to the red-shifting of the band gap previously reported when famatinite was doped on the Sb-site. Undoped famatinite produced by a solid-state process yielded a direct band gap of 0.88 eV, while Cu<sub>3</sub>Sb<sub>0.975</sub>Sn<sub>0.025</sub>S<sub>4</sub> demonstrated a direct band gap of 0.68 eV.66 This trend is continued for Bi and Sn codoping, where a direct band gap of 0.85 eV for  $Cu_3Sb_{0.98}Bi_{0.02}S_4$  was decreased to 0.73 eV for  $Cu_3Sb_{0.85}Bi_{0.06}Sn_{0.09}S_4.^{32}$  Doping on the Cu-site of other multinary chalcogenides, such as CZTS(e), has been shown to increase the band gap of the species.  $^{86,87}$  For example, Lidoping in  $(\text{Li}_x\text{Cu}_{1-x})_2\text{ZnSnSe}_4$  with x ranging from 0 to 0.12 widened the band gap from 1.05 to 1.18 eV, 86 while Ag-doping in  $(Cu_{1-x}Ag_x)_2ZnSnS_4$  with x between 0 and 1 increased the band gap from 1.5 to 2.01 eV.87,88 The findings here suggest that the band structure of famatinite is only slightly altered by Cu-site doping, and the distinctive nature of this famatinite system merits further investigation.

**Ligand Surface Functionalization.** Surface functionalization can be a valuable strategy to tune the surface properties to improve carrier transfer and nanoparticle dispersibility for solution-phase processability. To modify the surface properties

of the famatinite nanoparticles, alkanethiols were utilized for the sulfur coordination with the copper. Octadecanethiol (ODT) and 11-mercapto-1-undecanol (MUD) were chosen specifically for their difference in polarity given the methyl terminus of ODT and the hydroxyl terminus of MUD. The difference in polarity allowed for experimentation to test the surface functionalization through dispersion of the nanoparticles in three solvents of varying polarities: deionized water, ethanol, and n-hexane. The ODT and MUD coatings were completed via a facile procedure, and the coated nanoparticles will be referred to as ODT- and MUD-NPs, respectively. Also studied was the dispersion of control nanoparticles that were taken through the ligand functionalization process without the presence of a ligand. A small amount of each nanoparticle sample was dispersed in each of the solvents, and pictures were taken at set time intervals to investigate the solution-phase stability (Figure 6 and Figure S9).

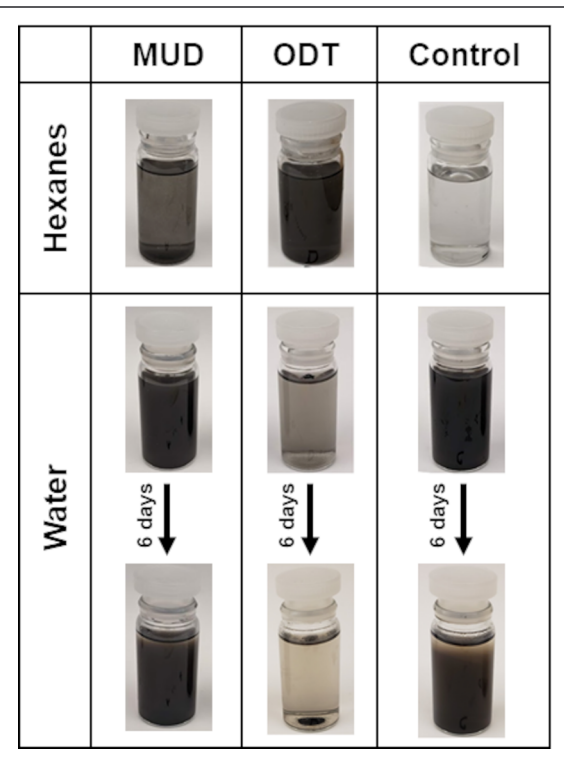


**Figure 6.** Famatinite nanoparticles with surface functionalization by 11-mercapto-1-undecanol (MUD) or 1-octadecanethiol (ODT) suspended by sonication in hexanes or water. Images of nanoparticles suspended in water after 6 days without agitation are also included. A sample of nanoparticles that underwent the surface functionalization process without an organic ligand present was tested as a control.

The hydrophobic coating of the ODT-NPs is successful in dispersing the nanoparticles in *n*-hexane (Figure 6). ODT-NPs are more stable than MUD-NPs, which are more stable than the control. MUD-NPs demonstrate a low capacity to disperse in *n*-hexane due to the exposed alkyl chain regions of their ligand shell. The control nanoparticle with no ligand coating shows no dispersibility in *n*-hexane. In deionized water, it is evident that MUD-NPs demonstrate high solution-phase stability, while ODT-NPs exhibit poor stability (Figure 6). MUD-NPs are stable in deionized water for more than 6 days. Control NPs behave similarly to the MUD-NPs in deionized water but drop out of the solution at a faster rate. ODT-NPs displayed little stability in deionized water and instead

clustered at the top and bottom of the solution. In ethanol, the dispersibility of the nanoparticles is high even without functionalization, but MUD functionalization can extend this suspension to several weeks (Figure S9). Figure S9 displays a full comparison of all nanoparticle and solvent combinations as a function of time, with the additional control of an "assynthesized" nanoparticle sample included. These nanoparticles were tested for solution-phase stability without any functionalization steps and were found to behave similarly to the control nanoparticles. In all cases, MUD-NPs remained dispersed longer in deionized water and ethanol than the controls or ODT-NPs. Conversely, ODT-NPs remained dispersed longer in *n*-hexane than the controls or MUD-NPs. This surface functionalization process was successful based on the significant stability differences between MUD-NPs, ODT-NPs, and control-NPs.

Conclusions and Future Directions. The modified polyol process has been shown to rapidly produce famatinite nanoparticles with high purity in a one-step and energyefficient synthesis. A synthetic optimization study determined the temperature and time to produce phase-pure famatinite. Addition of 10% mol excess sulfur in the synthesis improved the Cu and Sb EDS values to within 5% of the expected molar ratio, which is favorable in comparison to literature examples with Cu EDS ratios ranging from -16 to 48% of the target. 17,34,43,64 The modified polyol process demonstrated the capability to incorporate a wide range of dopants into famatinite on the Cu-site. Cu<sub>2.70</sub>Mn<sub>0.30</sub>SbS<sub>4</sub>, Cu<sub>2.70</sub>Ni<sub>0.30</sub>SbS<sub>4</sub>,  $Cu_{2,70}Zn_{0,30}SbS_4$ ,  $Cu_2ZnSbS_4$ , and  $Cu_{2,70}Fe_{0,30}SbS_4$  were produced phase-pure for the first time, with Mn and Fe doping having never been shown in the literature before. The tunability of Cu-site doping was shown for  $Cu_{3-x}Zn_xSbS_4$  (x =0.3, 0.6, 1) nanoparticles that were all produced with high purity. Doping on the Sb- and S-sites was also studied, and this paper reports the first incorporation of In, Bi, Sn, and Se by solution-phase methods. Synthesized nanoparticles were generally polycrystalline and nonuniform in shape with particle sizes that ranged from 20 to 30 nm. Thermal analysis of the undoped and doped famatinite nanoparticles showed that Mn and Zn doping improved the stability of the material by decreasing the amount of sulfur lost upon heating. A direct transition from famatinite to tetrahedrite was observed while annealing, highlighting the interplay between tetrahedrite and famatinite phases. While nanostructuring decreased the thermal stability of famatinite in comparison to bulk products studied in the literature, XRD analysis of annealing products suggests that nanostructured products could be annealed at up to 300 °C and maintain phase purity. Cu-site dopants, most notably Mn and Zn, improved thermal stability and maintained optical properties. Optical studies observed that all undoped and doped nanoparticles possess a direct band gap of 0.9 eV, which is in agreement with prior optical studies of undoped famatinite. The presence of the direct band gap in all samples suggests that the modified polyol method is predisposed to forming samples in which the direct transition is dominant, which is notable over other solution-phase methods. Postsynthetic surface functionalization studies demonstrated the promise of utilizing alkanethiols ligands to improve the processability of nanoparticles that could be spin-coated to create thin films.

Understanding the synthetic pathway, optical properties, thermal stability, and ligand functionalization of solution-phase famatinite nanoparticles is important for future applications in photovoltaics and thermoelectrics. Given that doping on the Cu-site is found to produce a direct ~1 eV band gap and benefit the thermal stability of the material, it is expected that these quaternary famatinites will have improved performance relative to undoped famatinite in photovoltaic devices. Poor band alignment between intrinsically p-type Cu<sub>3</sub>SbS<sub>4</sub> and commonly used n-type TiO2 is cited as a reason for the poor efficiency of famatinite-based photoelectrochemical devices. The tunability of Cu-site dopants evidenced herein suggests that famatinite could be doped sufficiently to exhibit an n-type behavior, which is of interest because n-type CAS phases are uncommon. This n-type behavior may occur due to divalent dopants on the monovalent Cu site in Cu<sub>3</sub>SbS<sub>4</sub>, which would increase electron contribution to the material.<sup>45</sup> For all famatinite nanoparticles, the thermal stability of famatinite is promising for incorporation into alternative energy applications with threshold temperatures below 300 °C, and the phase interchangeability between famatinite and tetrahedrite upon additional annealing is a synthetic approach for further exploration. Optimization and characterization of the other doped famatinite species represent another key avenue of research, as Sb- and S-site doping has not been systematically studied. Surface functionalization studies suggest that the processability of famatinite can be tailored, enabling facile thin film coating. Coating nanoparticles with conductive ligand shells is a prospect that may improve carrier transport properties for photovoltaic applications and negate the disadvantages of nanostructured photovoltaics. The expansion of synthetic strategies and dopant types serves to enable a greater degree of control over the properties of famatinite for enhanced performance in energy applications.

#### ASSOCIATED CONTENT

# Supporting Information

The Supporting Information is available free of charge at https://pubs.acs.org/doi/10.1021/acs.chemmater.2c01888.

EDS of temperature- and time-based growth mechanism; XRD of time-based growth mechanism; Rietveld refinements of undoped and doped famatinites; XRD and EDS of other undoped famatinite species produced by a modified polyol method; additional TEM images with particle size analysis of undoped and doped famatinites; replicates of TGA and DSC curves; Raman spectroscopy of undoped and doped famatinite; XRD of thermal annealed samples from 100 to 300 °C; EDS of thermal decomposition products; vis-IR absorbance spectra with Tauc plots; compilation table of optical properties and elemental analysis reported in the literature; and full representation of surface functionalization experiments (PDF)

# AUTHOR INFORMATION

#### **Corresponding Author**

Mary E. Anderson — Chemistry Department, Furman University, Greenville, South Carolina 29613, United States; orcid.org/0000-0001-8369-2177; Email: maryelizabeth.anderson@furman.edu

# **Authors**

Mitchel S. Jensen — Chemistry Department, Furman University, Greenville, South Carolina 29613, United States; orcid.org/0000-0002-8013-787X

Katherine E. Plass — Chemistry Department, Franklin & Marshall College, Lancaster, Pennsylvania 17604, United States; © orcid.org/0000-0002-4544-5471

Complete contact information is available at: https://pubs.acs.org/10.1021/acs.chemmater.2c01888

#### Notes

The authors declare no competing financial interest.

#### ACKNOWLEDGMENTS

Aspects of this work were supported by NSF Made in SC EPSCoR #OIA-1655740 (M.E.A., M.S.J.), NSF RUI CHM #1905221 (M.E.A.), NSF RUI DMR #2003337 (K.E.P.), and the Camille & Henry Dreyfus Foundation (M.E.A.). Additional support was provided by the Furman University Chemistry Department, Dr. Christopher Romanek, and Dr. Xuezhong He. For materials characterization support, work was undertaken at the Penn State University Materials Characterization Laboratory. Specifically, we acknowledge the contributions of Dr. Maxwell Wetherington for Raman characterization. We also acknowledge the contributions of Dr. Jennifer Gray and Haiying Wang for TEM characterization.

#### REFERENCES

- (1) Green, M.; Dunlop, E.; Hohl-Ebinger, J.; Yoshita, M.; Kopidakis, N.; Hao, X. Solar cell efficiency tables. *Prog. Photovolt.* **2019**, 28, 3.
- (2) Saga, T. Advances in crystalline silicon solar cell technology for industrial mass production. NPG Asia Mater. 2010, 2, 96.
- (3) Meillaud, F.; Boccard, M.; Bugnon, G.; Despeisse, M.; Hänni, S.; Haug, F. J.; Persoz, J.; Schüttauf, J. W.; Stuckelberger, M.; Ballif, C. Recent advances and remaining challenges in thin-film silicon photovoltaic technology. *Mater. Today* **2015**, *18*, 378.
- (4) Jackson, P.; Hariskos, D.; Wuerz, R.; Kiowski, O.; Bauer, A.; Friedlmeier, T. M.; Powalla, M. Properties of Cu(In,Ga)Se<sub>2</sub> solar cells with new record efficiencies up to 21.7%. *Phys. Status Solidi RRL* **2015**, *9*, 28.
- (5) Kamada, R.; Yagioka, T.; Adachi, S.; Handa, A.; Tai, K. F.; Kato, T. Sugimoto, H. New world record Cu(In, Ga)(Se, S)<sub>2</sub> thin film solar cell efficiency beyond 22%. *PVSC* **2016**, 1287.
- (6) Yan, C.; Huang, J.; Sun, K.; Johnston, S.; Zhang, Y.; Sun, H.; Pu, A.; He, M.; Liu, F.; Eder, K.; Yang, L.; Cairney, J. M.; Ekins-Daukes, N. J.; Hameiri, Z.; Stride, J. A.; Chen, S.; Green, M. A.; Hao, X. Cu<sub>2</sub>ZnSnS<sub>4</sub> solar cells with over 10% power conversion efficiency enabled by heterojunction heat treatment. *Nat. Energy* **2018**, *3*, 764.
- (7) Gokmen, T.; Gunawan, O.; Todorov, T. K.; Mitzi, D. B. Band tailing and efficiency limitation in kesterite solar cells. *Appl. Phys. Lett.* **2013**, *103*, 103506.
- (8) Bosson, C. J.; Birch, M. T.; Halliday, D. P.; Knight, K. S.; Gibbs, A. S.; Hatton, P. D. Cation disorder and phase transitions in the structurally complex solar cell material Cu<sub>2</sub>ZnSnS<sub>4</sub>. *J. Mater. Chem. A* **2017**, *5*, 16672.
- (9) Tan, G.; Shi, F.; Hao, S.; Zhao, L.; Chi, H.; Zhang, X.; Uher, C.; Wolverton, C.; Dravid, V. P.; Kanatzidis, M. G. Non-equilibrium processing leads to record high thermoelectric figure of merit in PbTe–SrTe. *Nat. Commun.* **2016**, *7*, 12167.
- (10) Kim, S. I.; Lee, K. H.; Mun, H. A.; Kim, H. S.; Hwang, S. W.; Roh, J. W.; Yang, D. J.; Shin, W. H.; Li, X. S.; Lee, Y. H.; Snyder, G. J.; Kim, S. Dense dislocation arrays embedded in grain boundaries for high-performance bulk thermoelectrics. *Science* **2015**, 348, 109.
- (11) Tan, G.; Zhao, L.-D.; Kanatzidis, M. G. Rationally Designing High-Performance Bulk Thermoelectric Materials. *Chem. Rev.* **2016**, 116, 12123.
- (12) Dughaish, Z. H. Lead telluride as a thermoelectric material for thermoelectric power generation. *Phys. B* **2002**, 322, 205.

- (13) Shi, X.-L.; Zou, J.; Chen, Z.-G. Advanced Thermoelectric Design: From Materials and Structures to Devices. *Chem. Rev.* **2020**, 120, 7399.
- (14) Rath, T.; MacLachlan, A. J.; Brown, M. D.; Haque, S. A. Structural, optical and charge generation properties of chalcostibite and tetrahedrite copper antimony sulfide thin films prepared from metal xanthates. *I. Mater. Chem. A* **2015**, *3*, 24155.
- (15) Zeng, Q.; Di, Y.; Huang, C.; Sun, K.; Zhao, Y.; Xie, H.; Niu, D.; Jiang, L.; Hao, X.; Lai, Y.; Liu, F. Famatinite Cu<sub>3</sub>SbS<sub>4</sub> nanocrystals as hole transporting material for efficient perovskite solar cells. *J. Mater. Chem. C* **2018**, *6*, 7989.
- (16) Tamilselvan, M.; Bhattacharyya, A. J. Tetrahedrite ( $Cu_{12}Sb_4S_{13}$ ) Ternary Inorganic Hole Conductor for Ambient Processed Stable Perovskite Solar Cells. *ACS Appl. Energy Mater.* **2018**, *1*, 4227.
- (17) Pi, J.-H.; Lee, G. E.; Kim, I.-H. Charge Transport and Thermoelectric Properties of Ge-Doped Famatinites Cu<sub>3</sub>Sb<sub>1-y</sub>Ge<sub>y</sub>S<sub>4</sub>. *Electron. Mater. Lett.* **2021**, *17*, 427.
- (18) Nagaoka, A.; Takeuchi, M.; Yoshino, K.; Ikeda, S.; Yasui, S.; Taniyama, T.; Nishioka, K. Growth of CuSbS<sub>2</sub> Single Crystal as an Environmentally Friendly Thermoelectric Material. *Phys. Status Solidi A* **2019**, *216*, 1800861.
- (19) Weller, D. P.; Stevens, D. L.; Kunkel, G. E.; Ochs, A. M.; Holder, C. F.; Morelli, D. T.; Anderson, M. E. Thermoelectric Performance of Tetrahedrite Synthesized by a Modified Polyol Process. *Chem. Mater.* **2017**, *29*, 1656.
- (20) Peccerillo, E.; Durose, K. Copper-antimony and copper-bismuth chalcogenides-Research opportunities and review for solar photovoltaics. *MRS Energy Sustain.* **2018**, *5*, 13.
- (21) Crespo, C. T. Microscopic Optical Absorption, Analysis, and Applications of Famatinite Cu<sub>3</sub>SbS<sub>4</sub>. *J. Phys. Chem. C* **2016**, 120, 7959.
- (22) Van Embden, J.; Latham, K.; Duffy, N. W.; Tachibana, Y. Near-Infrared Absorbing Cu<sub>12</sub>Sb<sub>4</sub>S<sub>13</sub> and Cu<sub>3</sub>SbS<sub>4</sub> Nanocrystals: Synthesis, Characterization, and Photoelectrochemistry. *J. Am. Chem. Soc.* **2013**, 135, 11562.
- (23) Yu, L.; Kokenyesi, R. S.; Keszler, D. A.; Zunger, A. Inverse Design of High Absorption Thin-Film Photovoltaic Materials. *Adv. Energy Mater.* **2013**, *3*, 43.
- (24) Amirkhanov, K. I.; Gadzhiev, G. G.; Magomedov, Y. B. Thermal conductivity of Cu<sub>3</sub>SbS<sub>4</sub> and Cu<sub>3</sub>AsS<sub>4</sub> compounds. *Teplofiz. Vyz. Temp.* **1978**, *16*, 1232.
- (25) Ramasamy, K.; Sims, H.; Butler, W. H.; Gupta, A. Selective Nanocrystal Synthesis and Calculated Electronic Structure of All Four Phases of Copper—Antimony—Sulfide. *Chem. Mater.* **2014**, *26*, 2891.
- (26) Zhang, Y.; Tian, J.; Jiang, K.; Huang, J.; Wang, H.; Song, Y. Gas—solid reaction for in situ deposition of Cu<sub>3</sub>SbS<sub>4</sub> on a mesoporous TiO<sub>2</sub> film. *RSC Adv.* **2017**, *7*, 41540.
- (27) Ghorpade, U. V.; Suryawanshi, M. P.; Shin, S.; Wang, X.; Jo, E.; Bae, H.; Park, K.; Ha, J.; Kolekar, S. S.; Kim, J. H. Eutectic solvent-mediated selective synthesis of Cu–Sb–S-based nanocrystals: combined experimental and theoretical studies toward highly efficient water splitting. *J. Mater. Chem. A* **2018**, *6*, 19798.
- (28) Chalapathi, U.; Poornaprakash, B.; Park, S.-H. Growth and properties of Cu<sub>3</sub>SbS<sub>4</sub> thin films prepared by a two-stage process for solar cell applications. *Ceram. Int.* **2017**, 43, 5229.
- (29) Han, G.; Lee, J. W.; Kim, J. Fabrication and Characterization of Cu<sub>3</sub>SbS<sub>4</sub> Solar Cell with Cd-free Buffer. *J. Korean Phys. Soc.* **2018**, 73, 1794.
- (30) Franzer, N. D.; Paudel, N. R.; Xiao, C.; Yan, Y. Study of RF sputtered Cu<sub>3</sub>SbS<sub>4</sub> thin-film solar cells. *PVSC* **2014**, 2326.
- (31) Albuquerque, G. H.; Kim, K.; Lopez, J. I.; Devaraj, A.; Manandhar, S.; Liu, Y.; Guo, J.; Chang, C.; Herman, G. S. Multimodal characterization of solution-processed Cu<sub>3</sub>SbS<sub>4</sub> absorbers for thin film solar cells. *J. Mater. Chem. A* **2018**, *6*, 8682.
- (32) Shen, M.; Lu, S.; Zhang, Z.; Liu, H.; Shen, W.; Fang, C.; Wang, Q.; Chen, L.; Zhang, Y.; Jia, X. Bi and Sn Co-doping Enhanced Thermoelectric Properties of Cu<sub>3</sub>SbS<sub>4</sub> Materials with Excellent Thermal Stability. ACS Appl. Mater. Interfaces 2020, 12, 8271.

- (33) Pi, J.; Lee, G.; Kiem, I. Effects of Sn-Doping on the Thermoelectric Properties of Famatinite. *J. Electron. Mater.* **2019**, 49, 2755.
- (34) Suzumura, A.; Watanabe, M.; Nagasako, N.; Asahi, R. Improvement in Thermoelectric Properties of Se-Free Cu<sub>3</sub>SbS<sub>4</sub> Compound. *J. Electron. Mater.* **2014**, *43*, 2356.
- (35) Goto, Y.; Sakai, Y.; Kamihara, Y.; Matoba, M. Effect of Sn-Substitution on Thermoelectric Properties of Copper-Based Sulfide, Famatinite Cu<sub>3</sub>SbS<sub>4</sub>. *J. Phys. Soc. Jpn.* **2015**, *84*, 44706.
- (36) Dutková, E.; Jesús Sayagués, M.; Fabián, M.; Baláž, M.; Achimovičová, M. Mechanochemically synthesized ternary chalcogenide Cu<sub>3</sub>SbS<sub>4</sub> powders in a laboratory and an industrial mill. *Mater. Lett.* **2021**, 291, 129566.
- (37) Bella, M.; Rivero, C.; Blayac, S.; Basti, H.; Record, M. C.; Boulet, P. Oleylamine-assisted solvothermal synthesis of copper antimony sulfide nanocrystals: Morphology and phase control. *Mater. Res. Bull.* **2017**, *90*, 188.
- (38) Baum, F.; Pretto, T.; Brolo, A. G.; Santos, M. J. L. Uncovering the Mechanism for the Formation of Copper Thioantimonate (Sb<sup>V</sup>) Nanoparticles and Its Transition to Thioantimonide (Sb<sup>III</sup>). *Cryst. Growth Des.* **2018**, *18*, 6521.
- (39) Bincy, J. Temperature dependent solvothermal synthesis of Cu-Sb-S nanoparticles with tunable structural and optical properties. *Mater. Res. Bull.* **2017**, *95*, 267.
- (40) Shi, L.; Wu, C.; Li, J.; Ding, J. Selective synthesis and photoelectric properties of Cu<sub>3</sub>SbS<sub>4</sub> and CuSbS<sub>2</sub> nanocrystals. *J. Alloys Compd.* **2017**, 694, 132.
- (41) Ikeda, S.; Sogawa, S.; Tokai, Y.; Septina, W.; Harada, T.; Matsumura, M. Selective production of CuSbS<sub>2</sub>, Cu<sub>3</sub>SbS<sub>3</sub>, and Cu<sub>3</sub>SbS<sub>4</sub> nanoparticles using a hot injection protocol. *RSC Adv.* **2014**, *4*, 40969.
- (42) Xu, B.; Zhang, X.; Sun, Y.; Zhang, J.; Wang, Y.; Yi, L. Elastic Anisotropy and Anisotropic Transport Properties of Cu<sub>3</sub>SbSe<sub>4</sub> and Cu<sub>3</sub>SbS<sub>4</sub>. *J. Phys. Soc. Jpn.* **2014**, *83*, 094606.
- (43) Lee, G.; Pi, J.; Kim, I. Preparation and Thermoelectric Properties of Famatinite Cu<sub>3</sub>SbS<sub>4</sub>. J. Electron. Mater. **2019**, 49, 2781.
- (44) Tanishita, T.; Suekuni, K.; Nishiate, H.; Lee, C.-H.; Ohtaki, M. A strategy for boosting the thermoelectric performance of famatinite Cu<sub>3</sub>SbS<sub>4</sub>. *Phys. Chem. Chem. Phys.* **2020**, 22, 2081.
- (45) Heppke, E. M.; Klenner, S.; Janka, O.; Pöttgen, R.; Bredow, T.; Lerch, M. Cu<sub>2</sub>ZnSbS<sub>4</sub>: A Thioantimonate(V) with Remarkably Strong Covalent Sb–S Bonding. *Inorg. Chem.* **2021**, *60*, 2730.
- (46) Suehiro, S.; Horita, K.; Yuasa, M.; Tanaka, T.; Fujita, K.; Ishiwata, Y.; Shimanoe, K.; Kida, T. Synthesis of Copper—Antimony-Sulfide Nanocrystals for Solution-Processed Solar Cells. *Inorg. Chem.* **2015**, *54*, 7840.
- (47) Fasana, C. D.; Jensen, M. S.; García Ponte, G. E.; MacAlister, T. R.; Kunkel, G. E.; Rogers, J. P.; Ochs, A. M.; Stevens, D.; Weller, D. P.; Morelli, D.; Anderson, M. E. Synthetic Versatility, Reaction Pathway, and Thermal Stability of Tetrahedrite Nanoparticles. *J. Mater. Chem. C* **2020**, *8*, 14219.
- (48) Lu, X.; Morelli, D. T.; Xia, Y.; Zhou, F.; Ozolins, V.; Chi, H.; Zhou, X.; Uher, C. High Performance Thermoelectricity in Earth-Abundant Compounds Based on Natural Mineral Tetrahedrites. *Adv. Energy Mater.* **2013**, *3*, 342.
- (49) Weller, D. P.; Kunkel, G. E.; Ochs, A. M.; Morelli, D. T.; Anderson, M. E. Observation of n-type behavior in Fe-doped tetrahedrite at low temperature. *Mater. Today Phys.* **2018**, *7*, 1.
- (50) James, D. J.; Lu, X.; Morelli, D. T.; Brock, S. L. Solvothermal Synthesis of Tetrahedrite: Speeding Up the Process of Thermoelectric Material Generation. *ACS Appl. Mater. Interfaces* **2015**, *7*, 23623.
- (51) Powell, A. V. Recent developments in Earth-abundant coppersulfide thermoelectric materials. *J. Appl. Phys.* **2019**, *126*, 100901.
- (52) Lai, W.; Wang, Y.; Morelli, D. T.; Lu, X. From Bonding Asymmetry to Anharmonic Rattling in Cu<sub>12</sub>Sb<sub>4</sub>S<sub>13</sub> Tetrahedrites: When Lone-Pair Electrons Are Not So Lonely. *Adv. Funct. Mater.* **2015**, 25, 3648.
- (53) Nagaoka, A.; Takeuchi, M.; Shigeeda, Y.; Kamimizutaru, K.; Yoshino, K.; Nishioka, K. Chalcostibite Single-Crystal CuSbS<sub>2</sub> as

- High-Performance Thermoelectric Material. Mater. Trans. 2020, 61, 2407.
- (54) Xu, D.; Shen, S.; Zhang, Y.; Gu, H.; Wang, Q. Selective Synthesis of Ternary Copper—Antimony Sulfide Nanocrystals. *Inorg. Chem.* **2013**, *52*, 12958.
- (55) Banu, S.; Ahn, S. J.; Ahn, S. K.; Yoon, K.; Cho, A. Fabrication and characterization of cost-efficient CuSbS<sub>2</sub> thin film solar cells using hybrid inks. *Sol. Energy Mater. Sol. Cells* **2016**, *151*, 14.
- (56) Zhang, J.; Wang, L.; Liu, M.; Wang, J.; Sun, K.; Yang, Y.; Hu, B.; Xu, J.; Su, T.; Du, B. Preparation and thermoelectric performance of tetrahedrite-like cubic Cu<sub>3</sub>SbS<sub>3</sub> compound. *J. Mater. Sci.: Mater. Electron.* **2021**, 32, 10789.
- (57) Nikolaidou, K.; Sarang, S.; Ghosh, S. Nanostructured photovoltaics. *Nano Futures* **2019**, *3*, 12002.
- (58) Kanatzidis, M. G. Nanostructured Thermoelectrics: The New Paradigm? *Chem. Mater.* **2010**, *22*, 648.
- (59) Garin, J.; Parthé, E. The crystal structure of Cu<sub>3</sub>PSe<sub>4</sub> and other ternary normal tetrahedral structure compounds with composition 1<sub>3</sub>S6<sub>4</sub>. *Acta. Cryst. B.* **1972**, 28, 3672.
- (60) Wuensch, B. J. The crystal structure of tetrahedrite, Cu<sub>12</sub>Sb<sub>4</sub>S<sub>13</sub>. Z. Krystallog. **1964**, 119, 437.
- (61) Takeuchi, Y.; Kudoh, Y.; Sato, G. The crystal structure of covellite CuS under high pressure up to 33 kbar. Z. Kristallog. 1985, 173, 119.
- (62) Dehlinger, U. VI. Über die Kristallstruktur der Antimonoxyde. Z. Krystallog. 1928, 66, 108.
- (63) Rahman, A. A.; Hossian, E.; Vaishnav, H.; Parmar, J. B.; Bhattacharya, A.; Sarma, A. Synthesis and characterization of CuSbS thin films grown by co-sputtering metal precursors and subsequent sulfurization. *Mater. Adv.* **2020**, *1*, 3333.
- (64) Van Embden, J.; Tachibana, Y. Synthesis and characterisation of famatinite copper antimony sulfide nanocrystals. *J. Mater. Chem.* **2012**, 22, 11466.
- (65) Anderson, M. E.; Bharadwaya, S. S. N.; Schaak, R. E. Modified polyol synthesis of bulk-scale nanostructured bismuth antimony telluride. *J. Mater. Chem.* **2010**, *2*, 8362.
- (66) Lu, B.; Wang, M.; Yang, J.; Hou, H.; Zhang, X.; Shi, Z.; Liu, J.; Qiao, G.; Liu, G. Dense twin and domain boundaries lead to high thermoelectric performance in Sn-doped Cu<sub>3</sub>SbS<sub>4</sub>. *Appl. Phys. Lett.* **2022**, *120*, 173901.
- (67) Lemoine, P.; Bourgès, C.; Barbier, T.; Nassif, V.; Cordier, S.; Guilmeau, E. High temperature neutron powder diffraction study of the Cu<sub>12</sub>Sb<sub>4</sub>S<sub>13</sub> and Cu<sub>4</sub>Sn<sub>7</sub>S<sub>16</sub> phases. *J. Solid State Chem.* **2017**, 247, 83.
- (68) Yamamoto, K.; Kashida, S. X-ray study of the average structures of Cu<sub>2</sub>Se and Cu<sub>1.8</sub>S in the room temperature and the high temperature phases. *J. Solid State Chem.* **1991**, 93, 202.
- (69) Kullerud, G.; Yund, R. A. The Ni-S System and Related Minerals. J. Petrol. 1962, 3, 126.
- (70) Lin, S.; Yang, H.; Su, Y.; Chang, K.; Yang, C.; Lin, S. CALPHAD-assisted morphology control of manganese sulfide inclusions in free-cutting steels. *J. Alloys Compd.* **2019**, 779, 844.
- (71) Dong, J.; Wei, Y.; Zhou, S.; Li, B.; Yang, Y.; Mclean, A. The Effect of Additives on Extraction of Ni, Fe and Co from Nickel Laterite Ores. *JOM* **2018**, *70*, 2365.
- (72) Blachnik, R.; Müller, A. The formation of  $Cu_2S$  from the elements: I. Copper used in form of powders. *Thermochim. Acta* **2000**, 361, 31.
- (73) Laudise, R. A.; Ballman, A. A. Hydrothermal synthesis of zinc oxide and zinc sulfide. *J. Phys. Chem.* **1960**, *64*, 688.
- (74) Okamoto, H. *Phase Diagrams for Binary Alloys. Desk Handbook;* ASM International: Materials Park, OH, 2000.
- (75) Tippireddy, S.; Chetty, R.; Naik, M. H.; Jain, M.; Chattopadhyay, K.; Mallik, R. C. Eelectronic and Thermoelectric Properties of Transition Metal Substituted Tetrahedrites. *J. Phys. Chem. C* 2018, 122, 8735.
- (76) Pi, J.; Lee, G.; Kim, I. Thermal Stability, Mechanical Properties and Thermoelectric Performance of  $Cu_{11}TrSb_4S_{13}$  (Tr = Mn, Fe, Co, Ni, Cu, and Zn). *J. Elec. Mater.* **2019**, *49*, 2710.

**Chemistry of Materials** Article pubs.acs.org/cm

- (77) Makuła, P.; Pacia, M.; Macyk, W. How To Correctly Determine the Band Gap Energy of Modified Semiconductor Photocatalysts Based on UV-Vis Spectra. J. Phys. Chem. Lett. 2018, 9, 6814.
- (78) Fernandes, P. A.; Shongalova, A.; Da Cunha, A. F.; Teixeira, J. P.; Leitão, J. P.; Cunha, J. M. V.; Bose, S.; Salomé, P. M. P.; Correia, M. R. Phase selective growth of Cu<sub>12</sub>Sb<sub>4</sub>S<sub>13</sub> and Cu<sub>3</sub>SbS<sub>4</sub> thin films by chalcogenization of simultaneous sputtered metal precursors. J. Alloys Compd. 2019, 797, 1359.
- (79) Cho, A.; Banu, S.; Kim, K.; Park, J. H.; Yun, J. H.; Cho, J.; Yoo, J. Selective thin film synthesis of copper-antimony-sulfide using hybrid ink. Sol. Energy 2017, 145, 42.
- (80) Chalapathi, U.; Poornaprakash, B.; Cui, H.; Park, S.-H. Twostage processed high-quality famatinite thin films for photovoltaics. Superlattices Microstruct. 2017, 111, 188.
- (81) Sugarthi, S.; Manikandan, V. S.; Harish, S.; Bakiyaraj, G.; Navaneethan, M. Study on electrochemical performance of temperature-dependent Cu-Sb-S system. J. Mater. Sci.: Mater. Electron. 2022, 33, 9650.
- (82) Wang, Q.; Li, J.; Li, J. Enhanced thermoelectric performance of Cu<sub>3</sub>SbS<sub>4</sub> flower-like hierarchical architectures composed of Cl doped nanoflakes via an in situ generated CuS template. Phys. Chem. Chem. Phys. 2018, 20, 1460.
- (83) Liang, Q.; Huang, K.; Ren, X.; Zhang, W.; Xie, R.; Feng, S. Synthesis of Cu-Sb-S nanocrystals: insight into the mechanism of composition and crystal phase selection. CrystEngComm 2016, 18,
- (84) Chen, K.; Zhou, J.; Chen, W.; Chen, Q.; Zhou, P.; Liu, Y. A green synthesis route for the phase and size tunability of copper antimony sulfide nanocrystals with high yield. Nanoscale 2016, 8,
- (85) Balow, R. B.; Miskin, C. K.; Abu-Omar, M. M.; Agrawal, R. Synthesis and Characterization of Cu<sub>3</sub>(Sb<sub>1-x</sub>As<sub>x</sub>)S<sub>4</sub> Semiconducting Nanocrystal Alloys with Tunable Properties for Optoelectronic Device Applications. Chem. Mater. 2017, 29, 573.
- (86) Cabas-Vidani, A.; Haass, S. G.; Andres, C.; Caballero, R.; Figi, R.; Schreiner, C.; Márquez, J. A.; Hages, C.; Unold, T.; Bleiner, D.; Tiwari, A. N.; Romanyuk, Y. E. High-Efficiency (Li<sub>x</sub>Cu<sub>1-x</sub>)<sub>2</sub>ZnSn-(S,Se)<sub>4</sub> Kesterite Solar Cells with Lithium Alloying. Adv. Energy Mater. 2018, 8, 1801191.
- (87) Morihama, M.; Gao, F.; Maeda, T.; Wada, T. Crystallographic and optical properties of Cu<sub>2</sub>Zn(Sn<sub>1-x</sub>Ge<sub>x</sub>)Se<sub>4</sub> solid solution. *Jpn. J.* Appl. Phys. 2014, 53, 04ER09.
- (88) Romanyuk, Y. E.; Haass, S. G.; Giraldo, S.; Placidi, M.; Tiwari, D.; Fermin, D. J.; Hao, X.; Xin, H.; Schnabel, T.; Kauk-Kuusik, M.; Pistor, P.; Lie, S.; Wong, L. H. Doping and alloying of kesterites. J. Phys. Energy 2019, 1, 44004.
- (89) Ghorpade, U. V.; Suryawanshi, M. P.; Shin, S. W.; Kim, J.; Kang, S. H.; Ha, J. S.; Kolekar, S. S.; Kiem, J. H. Unassisted visible solar water splitting with efficient photoelectrodes sensitized by quantum dots synthesized via an environmentally friendly eutectic solvent-mediated approach. J. Mater. Chem. A 2018, 6, 22566.

# **□** Recommended by ACS

# Cu<sup>+</sup> → Mn<sup>2+</sup> Energy Transfer in Cu, Mn Coalloyed Cs<sub>3</sub>ZnCl<sub>5</sub> **Colloidal Nanocrystals**

Ying Liu, Liberato Manna, et al.

SEPTEMBER 20, 2022

CHEMISTRY OF MATERIALS

READ 2

## Cu-Mo-S Mixed Chalcogenide Nanostructures for **Pseudocapacitive Applications**

Anirudha Karati, Joydip Joardar, et al.

JULY 19, 2022

ACS APPLIED NANO MATERIALS

READ 🗹

### Colloidal Synthesis and Photocatalytic Properties of Cu<sub>2</sub>NbS<sub>4</sub> and Cu<sub>3</sub>NbSe<sub>4</sub> Sulvanite Nanocrystals

Chen-Yu Chang, Daniela R. Radu, et al.

JUNE 24, 2022

ACS NANOSCIENCE AU

READ **C** 

# Ternary and Quaternary Nanocrystalline Cu-Based Sulfides as Perspective Antibacterial Materials Mechanochemically Synthesized in a Scalable Fashion

Matej Baláž, Peter Baláž, et al.

JULY 26, 2022

ACS OMEGA

READ **C** 

Get More Suggestions >